International Journal of Heat and Mass Transfer 52 (2009) 4175–4183

Contents lists available at ScienceDirect

International Journal of Heat and Mass Transfer

journal homepage: www.elsevier.com/locate/ijhmt

# The transient response of vascular composites cooled with grids and radial channels

K.-M. Wang [a], S. Lorente [b], A. Bejan [a,*]

[a] Duke University, Department of Mechanical Engineering and Materials Science, Durham, NC 27708-0300, USA
[b] Université de Toulouse, UPS, INSA, LMDC (Laboratoire Matériaux et Durabilité des Constructions), 135, avenue de Rangueil, F-31 077 Toulouse Cedex 04, France

ARTICLE INFO

*Article history:*
Received 26 February 2009
Received in revised form 17 April 2009
Accepted 17 April 2009
Available online 6 June 2009

*Keywords:*
Constructal
Vascular
Smart materials
Time-delayed cooling
Response time
Heat removal time
Hot volume fraction

ABSTRACT

Here we develop vasculatures for smart materials with volumetric cooling capability under time-varying conditions. The objective is for the vascularized composite to survive without coolant flow such that its peak temperature does not overshoot the maximum allowable level. The transient performance of four vasculatures is reported: grids (G) and radial channels (R), and two flow directions, inlet in the center (I) and outlet in the center (O). Designs with outlet in the center offer short response times when the Be number is smaller than $10^9$. Configurations with outlet in the center offer short heat removal times and small hot volume fractions.



## 1. Introduction

The tree through which water stops flowing becomes a piece of dead wood. The river that dries up becomes arid land that turns into desert. It is the flow that keeps all these "designed" systems alive. These flow architectures, however, are not random and arbitrary – they conform to patterns commonly referred to as rules, scaling, similarity and "design in nature" [1]. For these many phenomena of design generation in time, the constructal law [1,2] serves as unifying principle: "For a flow system to persist in time (to live) it must evolve in such a way that it provides easier and easier access to the currents that flow through it." This is the time direction of evolution as a universal phenomenon, from inanimate flow systems to animate, social and engineered. New work and methods for how to discover effective flow architectures are appearing in a variety of fields, from engineering [3–20] to geophysics, biology and social dynamics [1,2,21–23]. This work was reviewed most recently in Refs. [24,25].

The discovery of the relationship between the architecture of the flow system and its global performance is key. Among the newest trends is the development of new smart materials with designed vasculatures [1,26,27]. These new structures offer new volumetric functionalities: self-cooling, self-healing, variable transport properties, etc. The first prototype of smart materials with self-healing functionality is the design with embedded microcapsules of healing liquids such as epoxy [28]. When the material is overworked and tiny cracks appear in it, the microcapsules break and their healing agents fill, react and fuse the cracks. After a certain healing time the composite material regains its mechanical strength properties.

The use of microcapsules is a one-shot healing process. Needed is the capability to supply healing agents continuously (or on demand) throughout the volume of the material. This calls for the vascularization of the entire volume. Supply and evacuation networks are configured and distributed [1,26,27,29–32] in accordance with earlier constructal designs developed for the designed cooling performance [11–20,33–35]. The development of smart materials is marching toward smaller scales and greater interconnectedness between the small-scale details of the structure. This trend is in response to the need to install multiple functions throughout the material volume, for example, sensing, actuating, self-cooling and self-healing. In this direction, the designer of the morphing structure rediscovers the designs of nature: vascularized materials with tree-shaped flows, multiple functionality and unmatched robustness. The new smart materials look more and more like animal tissues because of the design-generation direction (cf. the constructal law), not because they are copied from nature.

In this paper we develop vasculatures for the smart materials with self-cooling functionality. These flow designs represent an important departure from the self-healing architectures developed in Refs. [26,27,29–32], where the sole objective of the flow architecture was to spread the flow as uniformly as possible throughout the volume. For self-cooling, the first function is to sense the excess

* Corresponding author. Tel.: +1 919 660 5309; fax: +1 919 660 8963.
*E-mail address:* abejan@duke.edu (A. Bejan).

0017-9310/$ - see front matter © 2009 Elsevier Ltd. All rights reserved.
doi:10.1016/j.ijheatmasstransfer.2009.04.021

**Nomenclature**

| | |
|---|---|
| Be | Bejan number, Eq. (23) |
| $c_p$ | specific heat at constant pressure, J kg$^{-1}$ K$^{-1}$ |
| $C$ | constant, Eq. (28) |
| $d_{g,r}$ | channel thickness, m |
| $D$ | scale of the channel diameter, m, Eq. (28) |
| $D_h$ | hydraulic diameter, m, Eq. (25) |
| $K$ | thermal conductivity, W m$^{-1}$ K$^{-1}$ |
| $L$ | side length of the square slab, m |
| $L_{g,r}$ | spacing between two ports on the perimeter, m |
| $n$ | normal direction |
| $N$ | number of channels, Eq. (28) |
| $P$ | pressure, Pa |
| Pr | Prandtl number, Eq. (22) |
| $q''$ | bottom heat flux, W m$^{-2}$ |
| Re | Reynolds number, Eq. (25) |
| Sv | svelteness number, Eq. (24) |
| $T$ | temperature, K |
| u, v, w | velocity components, m s$^{-1}$ |
| $V$ | total volume, m$^3$ |
| $V_f$ | total flow volume, m$^3$ |
| $x$, $y$, $z$ | Cartesian coordinates, m |

*Greek symbols*

| | |
|---|---|
| $\alpha$ | thermal diffusivity, m$^2$ s$^{-1}$ |
| $\Delta P$ | pressure difference, Pa |
| $\delta$ | penetration depth, m, Eq. (35) |
| $\varepsilon$ | excess heat removal time, Eq. (32) |
| $\phi$ | porosity |
| $\mu$ | dynamic viscosity, kg m$^{-1}$ s$^{-1}$ |
| $\nu$ | kinematic viscosity, m$^2$ s$^{-1;}$ |
| $\rho$ | density, kg m$^{-3}$ |
| $\sigma$ | hot volume fraction, Eq. (33) |
| $\tau$ | fraction of time constants, Eq. (31) |

*Subscripts*

| | |
|---|---|
| c | characteristic |
| d | delay |
| f | fluid |
| g | grid pattern |
| h | hydraulic |
| in | inlet |
| out | outlet |
| max | maximum |
| min | minimum |
| p | penetration |
| r | radial pattern |
| s | solid |
| ss | steady state |

*Superscripts*

| | |
|---|---|
| $(\sim)$ | dimensionless, Eqs. (9–13), (22) |

temperature that is harmful to the material and to suppress it. After the heating attack is detected, the flow of coolant is triggered. We are interested in the configurations that can respond to sudden intense heating in the shortest time. Two basic configurations are explored: grids and radial channels. Two characteristic times are defined to assist in the evaluation – the characteristic response time $\tilde{t}_{ss}$ and the heat removal time $\varepsilon$, Eqs. (26) and (32). Configurations with short $\tilde{t}_{ss}$ and $\varepsilon$ are sought. In addition, we document the evolution of the volume fraction of relatively hot material $\sigma$.

## 2. Numerical model and method

The vascularized composite body is a square slab of size $L \times L$ and thickness $0.1L$, which is heated from the bottom with a uniform heat flux $q''$ The other surfaces are adiabatic. Cooling is provided by an embedded three-dimensional channel network. Two architectures are modeled and compared: (a) grids and (b) radial channels, Fig. 1. The spacing between ports on the perimeter is fixed ($L_g = L_r$). The channel thicknesses of the grids and radial patterns are $d_g$ and $d_r$, respectively. Fig. 2 shows the embedded channels in greater detail, in only one eighth of the slab. The patterns of isotherms displayed in Figs. 1 and 2 are for the steady state, and their calculation is described in Section 3.

Two flow directions are considered, from the center of the slab to the periphery and from the periphery to the center. In total, four flow configurations are explored (see Fig. 1a and b):

GI, grids with inlet in the center;
GO, grids with outlet in the center;
RI, radial channels with inlet in the center;
RO, radial channels with outlet in the center.

Several quantities are fixed: the volume of the slab $V$, the total volume of the flow channels $V_f$ (or the porosity $\phi = V_f/V$), and the pressure difference between the inlet and the outlet ($\Delta P$).

We are interested in flow configurations that can remove excess heat in the shortest time. To achieve this, we simulated numerically the time-dependent fluid flow and temperature fields throughout the volume occupied by solid and flow channels. The conservation equations for mass and momentum are

$$\frac{\partial u}{\partial x}+\frac{\partial v}{\partial y}+\frac{\partial w}{\partial z}=0 \tag{1}$$

$$\rho\left(\frac{\partial u}{\partial t}+u\frac{\partial u}{\partial x}+v\frac{\partial u}{\partial y}+w\frac{\partial u}{\partial z}\right)=-\frac{\partial P}{\partial x}+\mu\nabla^2 u \tag{2}$$

$$\rho\left(\frac{\partial v}{\partial t}+u\frac{\partial v}{\partial x}+v\frac{\partial v}{\partial y}+w\frac{\partial v}{\partial z}\right)=-\frac{\partial P}{\partial y}+\mu\nabla^2 v \tag{3}$$

$$\rho\left(\frac{\partial w}{\partial t}+u\frac{\partial w}{\partial x}+v\frac{\partial w}{\partial y}+w\frac{\partial w}{\partial z}\right)=-\frac{\partial P}{\partial z}+\mu\nabla^2 w \tag{4}$$

where $\nabla^2=\partial^2/\partial x^2+\partial^2/\partial y^2+\partial^2/\partial z^2$. The conservation of energy in fluid and solid spaces requires

$$\frac{\partial T}{\partial t}+u\frac{\partial T}{\partial x}+v\frac{\partial T}{\partial y}+w\frac{\partial T}{\partial z}=\alpha_f\nabla^2 T \tag{5}$$

$$\frac{\partial T}{\partial t}=\alpha_s\nabla^2 T \tag{6}$$

where $\alpha_f$ and $\alpha_s$ are thermal diffusivities of fluid and solid, respectively. The heat flux imposed from the bottom is

$$q''=-k_s\frac{\partial T}{\partial z} \tag{7}$$

where $k_s$ is thermal conductivity of solid. The continuity of heat flux across the solid–fluid interfaces is expressed by

$$k_s\left.\frac{\partial T}{\partial n}\right|_s=k_f\left.\frac{\partial T}{\partial n}\right|_f \tag{8}$$

where $k_f$ is fluid thermal conductivity, and $n$ is the vector normal to the surface. The governing equations were nondimensionalized by defining the dimensionless variables

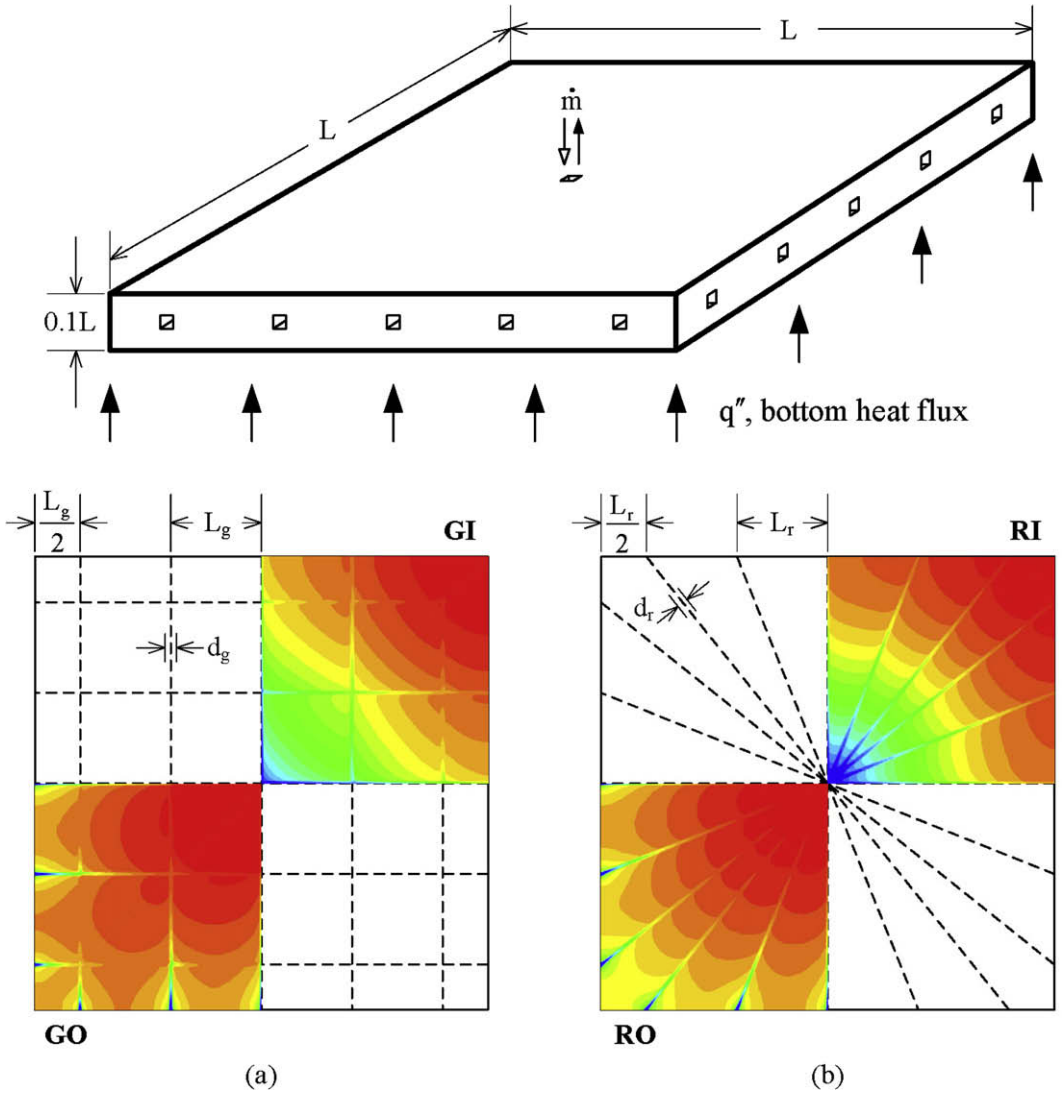


**Fig. 1.** Slab heated with uniform flux from below: (a) Grid channels, (b) Radial channels. Steady state temperature distributions in the middle planes of the slabs ($Be = 10^{10}$).

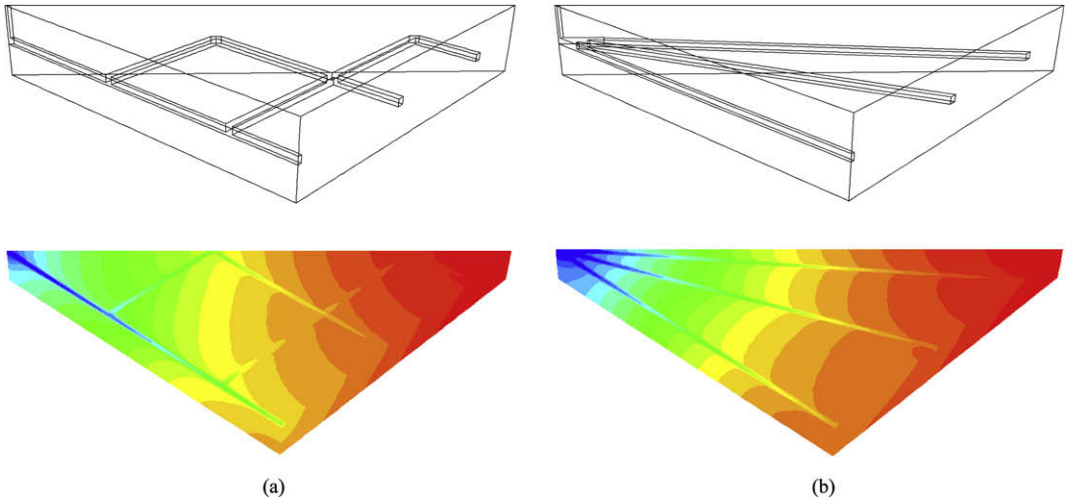


**Fig. 2.** One eighth of a square slab with embedded channels: (a) Grid channels, (b) Radial channels. The center of the slab is in the upper-left corner. Steady state temperature distributions over the surfaces of the bottom half of the slab ($Be = 10^{10}$).

$$\left(\tilde{x},\tilde{y},\tilde{z},\tilde{n},\tilde{L}_{g,r},\tilde{d}_{g,r}\right)=(x,y,z,n,L_{g,r},d_{g,r})/L \tag{9}$$

$$(\tilde{u},\tilde{v},\tilde{w})=(u,v,w)L/\alpha_f,\quad \tilde{P}=(P-P_{out})L^2/(\mu\alpha_f) \tag{10,11}$$

$$\tilde{T}=(T-T_{in})k_f/(q''L),\quad \tilde{t}=t\alpha_f/L^2 \tag{12,13}$$

where $P_{out}$ is the lowest pressure (at the outlets), and $T_{in}$ is the lowest temperature (the bulk fluid temperature at the inlets). Written in terms of dimensionless variables, Eqs. (1)–(8) become

$$\frac{\partial\tilde{u}}{\partial\tilde{x}}+\frac{\partial\tilde{v}}{\partial\tilde{y}}+\frac{\partial\tilde{w}}{\partial\tilde{z}}=0 \tag{14}$$

$$\frac{1}{\mathrm{Pr}}\left(\frac{\partial\tilde{u}}{\partial\tilde{t}}+\tilde{u}\frac{\partial\tilde{u}}{\partial\tilde{x}}+\tilde{v}\frac{\partial\tilde{u}}{\partial\tilde{y}}+\tilde{w}\frac{\partial\tilde{u}}{\partial\tilde{z}}\right)=-\frac{\partial\tilde{P}}{\partial\tilde{x}}+\nabla^2\tilde{u} \tag{15}$$

$$\frac{1}{\mathrm{Pr}}\left(\frac{\partial\tilde{v}}{\partial\tilde{t}}+\tilde{u}\frac{\partial\tilde{v}}{\partial\tilde{x}}+\tilde{v}\frac{\partial\tilde{v}}{\partial\tilde{y}}+\tilde{w}\frac{\partial\tilde{v}}{\partial\tilde{z}}\right)=-\frac{\partial\tilde{P}}{\partial\tilde{y}}+\nabla^2\tilde{v} \tag{16}$$

$$\frac{1}{\mathrm{Pr}}\left(\frac{\partial\tilde{w}}{\partial\tilde{t}}+\tilde{u}\frac{\partial\tilde{w}}{\partial\tilde{x}}+\tilde{v}\frac{\partial\tilde{w}}{\partial\tilde{y}}+\tilde{w}\frac{\partial\tilde{w}}{\partial\tilde{z}}\right)=-\frac{\partial\tilde{P}}{\partial\tilde{z}}+\nabla^2\tilde{w} \tag{17}$$

$$\frac{\partial\tilde{T}}{\partial\tilde{t}}+\tilde{u}\frac{\partial\tilde{T}}{\partial\tilde{x}}+\tilde{v}\frac{\partial\tilde{T}}{\partial\tilde{y}}+\tilde{w}\frac{\partial\tilde{T}}{\partial\tilde{z}}=\nabla^2\tilde{T} \tag{18}$$

$$\frac{\partial\tilde{T}}{\partial\tilde{t}}=\tilde{\alpha}\nabla^2\tilde{T} \tag{19}$$

$$1=-\tilde{k}\frac{\partial\tilde{T}}{\partial\tilde{z}},\quad \tilde{k}\frac{\partial\tilde{T}}{\partial\tilde{n}}\bigg|_s=\frac{\partial\tilde{T}}{\partial\tilde{n}}\bigg|_f \tag{20,21}$$

where the dimensionless groups are

$$\mathrm{Pr}=\frac{\nu}{\alpha_f},\quad \tilde{\alpha}=\frac{\alpha_s}{\alpha_f},\quad \tilde{k}=\frac{k_s}{k_f} \tag{22}$$

The imposed pressure difference $(P_{in}-P_{out})$ gives rise to the dimensionless group,

$$\mathrm{Be}=\frac{(P_{in}-P_{out})L^2}{\mu\alpha_f} \tag{23}$$

which is the Bejan number introduced by Bhattacharjee and Grosshandler [36] (see also Petrescu [37]).

The computations were performed using a finite-volume package [38] with first order implicit scheme for unsteady formulation, coupled algorithm for pressure–velocity coupling and second order upwind scheme for the energy and momentum equations. The independence of the solution with respect to the grid size was verified by examining the values of the total mass flow rate and the maximum temperature when the transient solutions reached steady state. The number of cells was increased in steps of 20% until the changes in the total mass flow rate and the maximum temperature were less than 1%. The nonuniform grid was denser in regions where the temperature and velocity fields had greater curvature. The residuals of the mass continuity, momentum and energy equations were less than $10^{-5}$. The number of grid cells varied from case to case; for example, the smallest number of cells ($5\times10^5$) was for a vascular design with radial channels, inlet in the center and Be = $5\times10^8$.

## 3. Time-dependent conjugate heat transfer

The numerical simulations were conducted in the dimensionless parametric domain Be = $10^8$–$10^{10}$, Pr = 6, $\tilde{\alpha}=58$ and $\tilde{k}=18$. These dimensionless groups represent a physical system that consists of epoxy as solid and water as fluid in the dimensional domain $L\sim5$ cm, $\Delta P\sim5$–500 Pa, $q''\sim10^3$–$10^5$ W/m$^2$ and hot spot excess temperatures of order $10^2$ K.

Because the total volume and the flow channel volume are fixed, the porosity ($\phi=V_f/V$) is also fixed. The numerical results illustrated in this paper are for $\phi=0.01$. The corresponding svelteness number Sv equals 10. The svelteness [1,39] is a global property of the flow architecture,

$$\mathrm{Sv}=\frac{\text{external flow length scale}}{\text{internal flow length scale}}=\frac{L}{V_f^{1/3}} \tag{24}$$

It was shown in [39] that when Sv is greater than 10 the pressure losses that occur at junctions are negligible in comparison with the pressure losses distributed along the channels. In the numerical simulations reported here the junction losses are not negligible. The Be range of these simulations correspond to channels with water flow at Reynolds numbers in the range 5–300. The Reynolds number is based on the hydraulic diameter of the channel $D_h$,

$$\mathrm{Re}=\frac{\rho UD_h}{\mu} \tag{25}$$

For each of the four configurations we started the numerical simulation from a state of uniform minimum temperature $\tilde{T}=0$, with stagnant isothermal fluid in all the channels. Beginning with $\tilde{t}=0$, a uniform heat flux $q''$ is applied and maintained on the bottom surface. Fig. 3 shows the evolution of the peak temperature $\tilde{T}=\tilde{T}_{max}$ of the configuration GI when Be = $10^9$. The peak temperature is located in the vicinity of corners, but the location of the hot spot is not as important as its temperature level. We are interested in two features:

(i) The time interval that the peak temperature needs in order to reach steady state.
(ii) The final steady state temperature $\tilde{T}=\tilde{T}_{max,ss}$.

In the example of Fig. 3 the peak temperature reaches steady state at $\tilde{t}=0.06$. We define the characteristic response time as the time when $\tilde{T}_{max}$ reaches 90% of $\tilde{T}_{max,ss}$,

$$\tilde{T}_{max}(\tilde{t}_{ss})=0.9\tilde{T}_{max,\,ss} \tag{26}$$

The characteristic response time $\tilde{t}_{ss}$ is plotted against the imposed pressure difference (Be) in Fig. 4. Effective cooling calls for designs with fast response, i.e. short $\tilde{t}_{ss}$ values. The response is fast

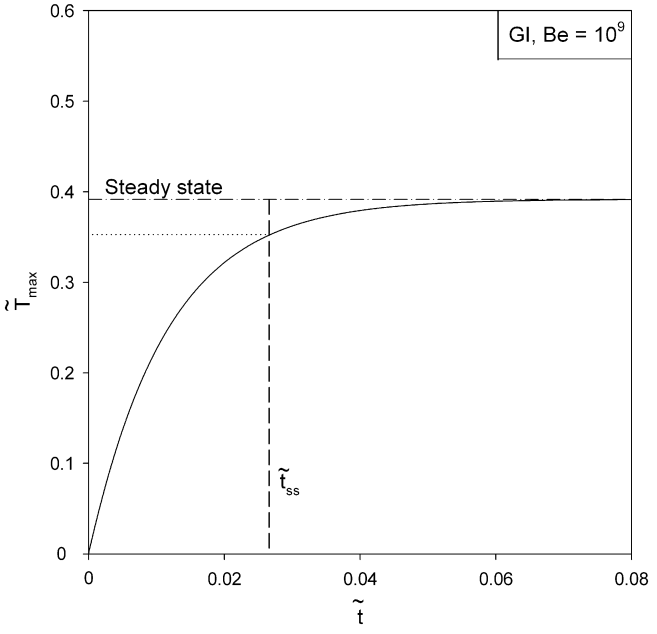


**Fig. 3.** The time evolution of the peak temperature $\tilde{T}_{max}$ (GI, Be = $10^9$).

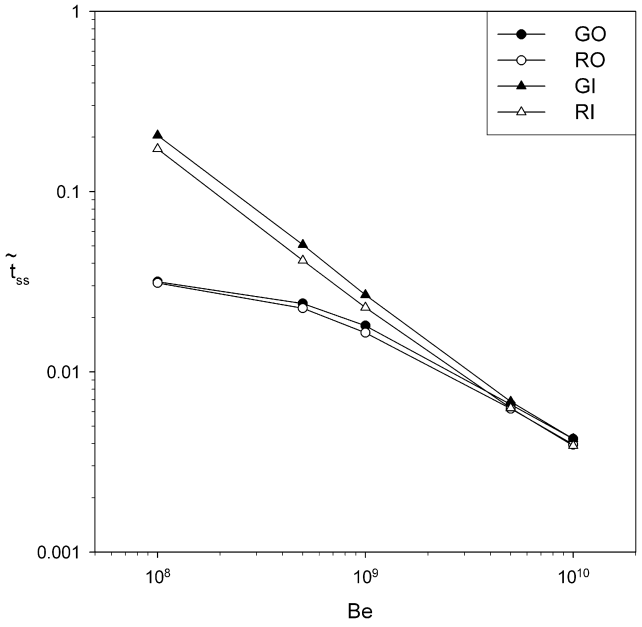


**Fig. 4.** The characteristic time $\tilde{t}_{ss}$ as a function of the dimensionless pressure difference Be.

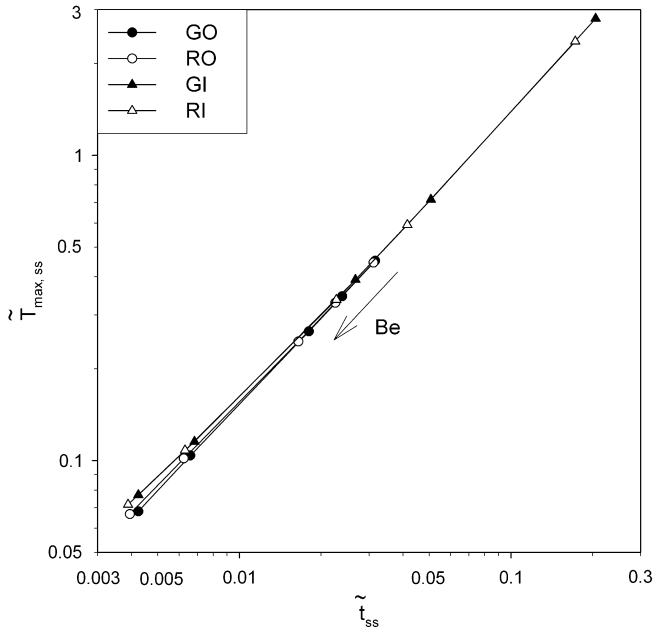


**Fig. 5.** The variation of the steady state peak temperature $\tilde{T}_{max,ss}$ with respect to the characteristic time $\tilde{t}_{ss}$.

when the pressure difference Be is large, and in this limit $\tilde{t}_{ss}$ decreases almost in proportion with $Be^{-1}$.

Fig. 4 documents further the effect of the flow configuration on the characteristic response time. When Be is less than $10^9$, the shorter $\tilde{t}_{ss}$ values are offered by the configurations with outlet in the center, and their characteristic response time is relatively insensitive to Be. This means that the response time is governed by the thermal diffusion across the slab, not by convection along the $L$ scale. When Be is greater than $10^9$, the difference of the response of designs with outlet in the center (GO, RO) and designs with inlet in the center (GI, RI) vanishes, and the cooling response time is governed by convection.

Fig. 5 shows that the steady state level reached by the peak temperature is proportional to the time of approach to steady state. The relationship is approximately $\tilde{T}_{max,ss} \cong 15\tilde{t}_{ss}$ for the four configurations. Such a proportionality can be anticipated based on energy conservation and scale analysis. The total heat transfer administered to the slab during the time $t_{ss}$ is $q''L^2t_{ss}$. The increase in the internal energy of the slab is $\left(\rho L^2 0.1L\right)c_P(T_{max,\,ss} - T_{in})$. By setting the two scales equal, we obtain $\tilde{T}_{max,\,ss} \sim 10\tilde{t}_{ss}$. The factor of order 10 (more precisely, 15, in Fig. 5) is due to the thinness of the slab used in the present simulations, slab length/thickness = 10. This scale-analysis prediction is valid provided that the heat convected away $\dot{m}c_P(T_{max,\,ss} - T_{in})t_{ss}$ is small relative to the heat input $q''L^2t_{ss}$.

$$\dot{m}c_P(T_{max,\,ss} - T_{in})t_{ss} < q''L^2t_{ss} \tag{27}$$

We confirm this by combining Eq. (27) with the scaling law for laminar flow in every channel

$$\Delta P \sim C\frac{\nu\dot{m}}{N}\frac{L}{D^4} \tag{28}$$

where $\dot{m}$ is the total mass flow rate, $N$ is the number of channels in an order of magnitude sense, and $D$ is the scale of the channel diameter. The factor $C$ is a numerical constant of order 10. The fixed flow volume fraction $\phi$ provides a relation between $N$ and $D$,

$$\phi \sim \frac{ND^2L}{L^2 0.1L} \tag{29}$$

Eliminating $\dot{m}$ between Eqs. (27) and (28), and using the definitions (12) and (23) we obtain

$$\tilde{T}_{max,\,ss}\mathrm{Be} < \frac{CN}{(0.1\phi)^2} \tag{30}$$

This inequality is respected in the present numerical simulations, because $C \sim 10$, $N \sim 10$ and $\phi = 0.01$, such that $CN/(0.1\phi)^2$ is of order $10^8$.

## 4. Time delay before the coolant starts flowing

In practice the implementation of vascular cooling also requires a system of sensing the start of uniform heating at $\tilde{t} = 0$, and then triggering the pumping of coolant. A time delay $\tilde{t}_d$ separates the initiation of convection cooling from the start of heating. In the preceding section the time delay was zero. In this section the time delay has a finite value that can be varied by design. At $\tilde{t} = 0$, the heat flux $q''$ is applied on a slab that is not bathed by the coolant (the channels are filled with stagnant coolant). At $\tilde{t} = \tilde{t}_d$, the coolant starts to flow and, in time, the flow approaches a fully developed flow.

First, we determined the characteristic time of the vascular system – the thermal inertia time, or time constant $\tilde{t}_c$ – as shown in Fig. 6. If the coolant is not flowing, then shortly after $\tilde{t} = 0$ the peak temperature of the system increases linearly in time. The system is also characterized by its steady state peak temperature $\tilde{T}_{max,ss}$, which occurs late enough when the coolant is flowing steadily. The intersection of the two lines defines the time constant identified as $\tilde{t}_c$ in Fig. 6. This is the same time scale as the warm up time $\tilde{t}_{ss}$ discussed above Eq. (27).

The time delay before the start of coolant is measured in dimensionless terms as the ratio

$$\tau = \frac{\tilde{t}_d}{\tilde{t}_c} \tag{31}$$

We simulated the thermal behavior of the vascular systems under six scenarios, $\tau = 0$, 0.5, 0.75, 0.85, 0.9 and 0.95. The $\tau = 0$ case means that the coolant is not flowing before $\tilde{t} = 0$ and that

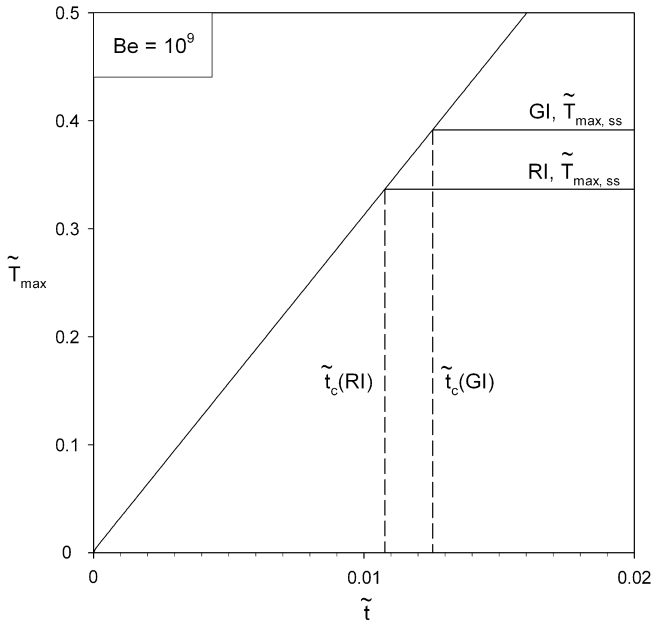


**Fig. 6.** The definition of the thermal inertia time $\tilde{t}_c$ of the vascular system.

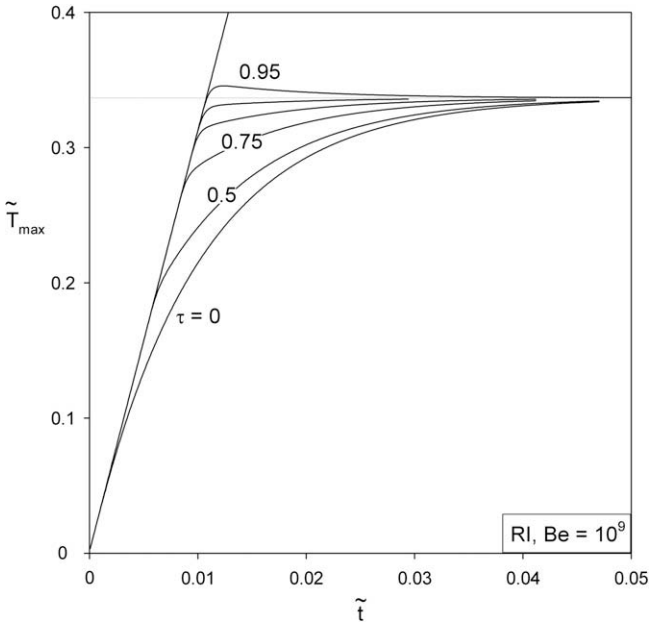


**Fig. 8.** The time evolution of the peak temperature $\tilde{T}_{max}$ of different coolant time delay values $\tau$ (RI design, Be = $10^9$).

immediately after $\tilde{t} = 0$ the fluid flow is developing en route to steady flow. We found that in both configurations with inlet in the center (GI, RI) the total inlet mass flow rate of coolant requires 3 time steps to reach steady state (one time step is $\Delta t = 1$ s, or dimensionless $\Delta\tilde{t} = 5.89 \times 10^{-5}$).

Figs 7 and 8 show the time evolution of $\tilde{T}_{max}$ for the GI and RI configurations when Be = $10^9$. Important is that when the delay time $\tau$ is larger than a critical value (called $\tau^*$), the peak temperature overshoots the steady state level. In practice, the overshoot must be avoided so that the peak temperature worthiness of the vascular design continues to be described by the steady state peak temperature. The longer the time interval in which the vascular design is safe to operate *without* coolant flowing, the shorter the excess heat removal time. A large $\tau^*$ (or $\tilde{t}_d^*$) value is attractive in the heat removal time comparison, provided that $\tilde{t}_c$ is a constant for all competing configurations. In this study $\tilde{t}_c$ varies from case to case indicating that the parameter $\tau^*$ (or $\tilde{t}_d^*$) is not sufficient for the heat removal time comparison. For example, in Table 1 we showed the $\tau^*$, $\tilde{t}_d^*$ and $\tilde{t}_c$ values of the GI configuration when Be = $10^8$ and $10^{10}$; Intuitively, because the flow network architecture does not change, with Be = $10^{10}$ we can keep the coolant stagnant longer than with Be = $10^8$. However, Table 1 showed that Be = $10^8$ has noticeably larger $\tau^*$ and $\tilde{t}_d^*$ values than Be = $10^{10}$, and this is the result of having different $\tilde{t}_c$ values. Hence, the time for the removal of excess heat is more suitable for discussion,

$$\varepsilon = \tilde{t}_c - \tilde{t}_d^* \tag{32}$$

The value of $\tau$ is still useful as it provides a systematic approach for the search of $\varepsilon$ values.

In the examples provided in Figs. 7 and 8, the critical $\tau$ values are $\tau^* = 0.92$ and 0.91, and the corresponding heat removal times are $\varepsilon = 10^{-3}$ and $9.7 \times 10^{-4}$. We performed a large number of simulations to discover how the heat removal time $\varepsilon$ varies with Be and the flow configurations. The results are presented in Fig. 9. Configurations with small $\varepsilon$ values are preferred. The designs with outlet in the center dramatically outperform the designs with inlet in the center. Among the four configurations, the grid with outlet in the center is the most effective design. The heat removal time $\varepsilon$ decreases as the pressure difference Be increases, provided that the design with inlet in the center is used. For designs with outlet in the center, $\varepsilon$ decreases as Be increases when Be is greater than $10^9$; furthermore, the Be value has a minor effect on the heat removal rates if the flow system cannot maintain a pressure difference higher than $10^9$.

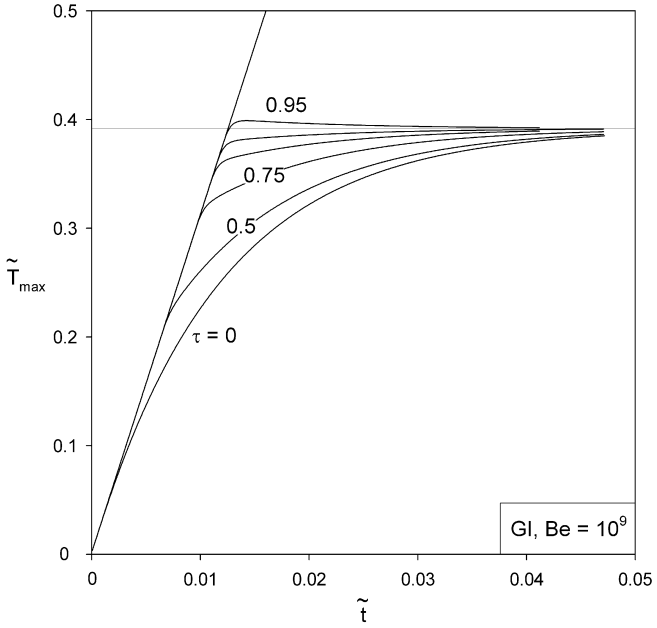


**Fig. 7.** The time evolution of the peak temperature $\tilde{T}_{max}$ of different coolant time delay values $\tau$ (GI design, Be = $10^9$).

**Table 1**
The $\tilde{t}_c$ effect on the inadequate usage of $\tau^*$ and $\tilde{t}_d^*$ for the heat removal time discussion.

| | $\tau^*$ | $\tilde{t}_d^*$ | $\tilde{t}_c$ |
|---|---|---|---|
| Be = $10^8$ | 0.98 | $8.8 \times 10^{-2}$ | $9 \times 10^{-2}$ |
| Be = $10^{10}$ | 0.73 | $1.76 \times 10^{-3}$ | $2.4 \times 10^{-3}$ |

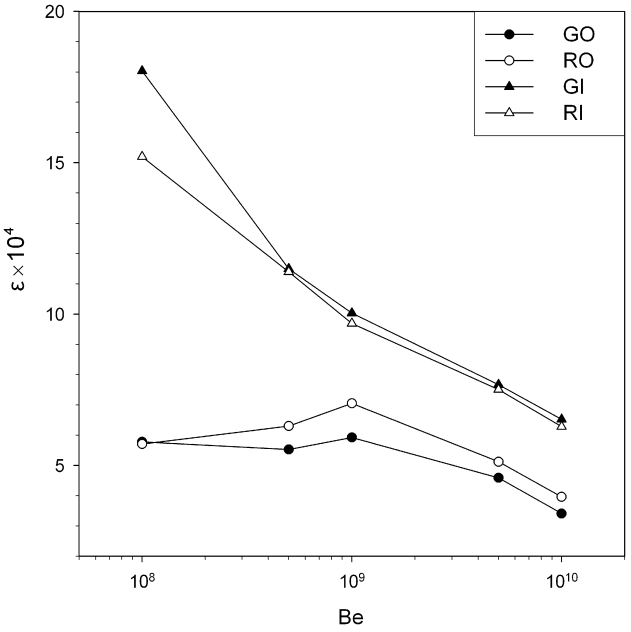


**Fig. 9.** The comparison of the excess heat removal time $\varepsilon$ of four configurations at different Be values.

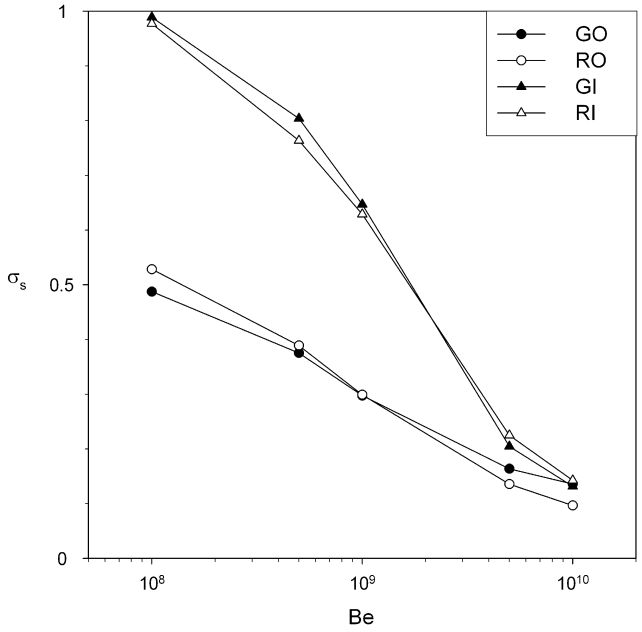


**Fig. 10.** The hot volume fraction of the solid domain of four configurations at five Be values.

## 5. Time evolution of the hot volume fraction

The cooling performance of flow configurations can be evaluated by monitoring their temperature distribution and hot volume fraction. We discussed the temperature distribution in Sections 3 and 4. In this section we will report the hot volume fraction, which is defined as

$$\sigma = \frac{V_{\text{hot}}}{V} \tag{33}$$

where $V_{\text{hot}}$ is the volume of material with temperatures between $\tilde{T}_{\max}$ and $\tilde{T}_{\text{hot}}$ $\left(\tilde{T}_{\text{hot}} < \tilde{T} < \tilde{T}_{\max}\right)$ such that $\tilde{T}_{\text{hot}}$ approaches $\tilde{T}_{\max}$ within 10 percent,

$$\frac{\tilde{T}_{\max} - \tilde{T}_{\text{hot}}}{\tilde{T}_{\max} - \tilde{T}_{\min}} \leqslant 0.1 \tag{34}$$

Consider first the distribution of the hot volume (the solid volume $\sigma_s$ and the fluid volume $\sigma_f$) of each configuration when the transient simulations reach steady state. The hot volume fractions $\sigma_s$ and $\sigma_f$ are determined by substituting local values of $\tilde{T}_{\max}$, $\tilde{T}_{\min}$ and $\tilde{T}_{\text{hot}}$ in the solid and fluid domains in Eq. (34). The results obtained for the hot volume fraction of the solid domain are shown in Fig. 10. We see that when Be is smaller than $10^{10}$ the designs with outlet in the center have smaller $\sigma_s$ values than the designs with inlet in the center. Smaller $\sigma_s$ values are more advantageous for the safe operation and mechanical worthiness of the solid structure. Fig. 10 also shows that the choice between grids and radial channels is minor. The more effective way to reduce the hot volume fraction is to orient the flow from the periphery to the center (GO and RO). The hot volume fractions in the fluid domain is reported in Fig. 11. When the inlet is in the center, radial patterns have smaller hot volume fractions. The grids are desired configurations provided that the outlet is located in the center.

The time evolution of hot volume fractions of two configurations (GI and RI, Be = $10^9$) is shown in Figs. 12 and 13. The hot volume fraction of the fluid domain is generated by two mechanisms, convection and conduction. As shown in Figs. 12 and 13, the hot volume fraction of the fluid volume $\sigma_f$ rises in 6 time steps and reaches a maximum, after which it converges to the steady state. These first steps account for the transient convection of the flow of fluid and heat. Later, the heat penetrates the flow network and the hot volume fraction converges to the steady state value.

We defined $\tilde{t}_{\sigma,\text{ss}}$ as the time when $\sigma$ reaches 90% of the steady state value. We compared $\tilde{t}_{\text{ss}}$ with the time $\tilde{t}_{\sigma,\text{ss}}$ discussed in Section 3 in Table 2. The results show that $\sigma_{s,\,f}$ reaches steady state much faster than $\tilde{T}_{\max}$. This is due to the fact that the evolution of the hot volume fraction is ruled by the penetration of heat through the slab. The penetration time for the solid volume of the slab is

$$t_p \sim \frac{\delta^2}{\alpha} \tag{35}$$

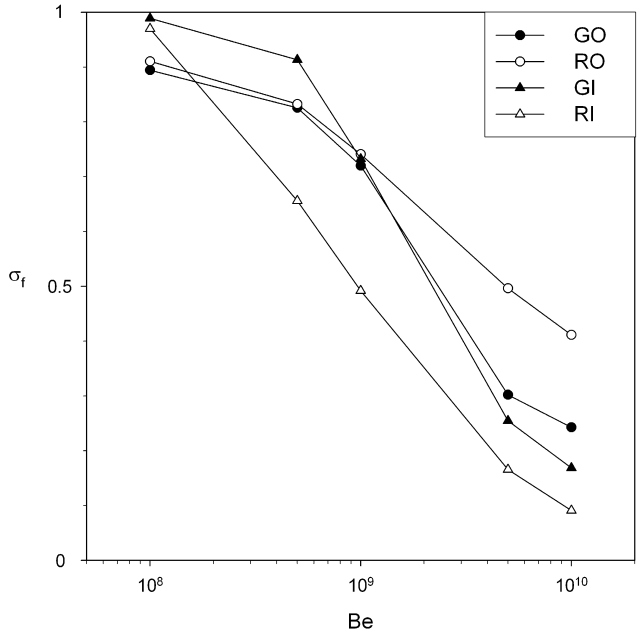


**Fig. 11.** The hot volume fraction of the fluid domain of four configurations at five Be values.

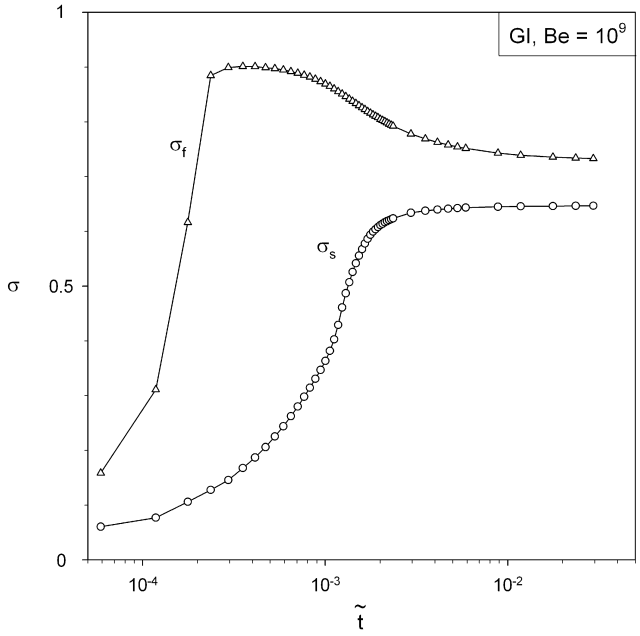


**Fig. 12.** The time evolution of the hot volume fraction of the GI configuration when Be = $10^9$.

where $\delta$ is the penetration depth. Eq. (35) was nondimensionalized by using Eqs. (13), Eq. (22) and $\tilde{\delta} = \delta/L$,

$$\tilde{t}_p \sim \frac{\tilde{\delta}^2}{\tilde{\alpha}} \tag{36}$$

If the heat penetrates directly from the bottom surface to the top plane, then if we substitute $\tilde{\delta} = 0.1$ in Eq. (36), we obtain the penetration time $\tilde{t}_p = 1.72 \times 10^{-4}$ Substituting $\tilde{\delta} = 0.5$ in Eq. (36) yields the penetration time from the periphery to the center, which is $\tilde{t}_p = 4.3 \times 10^{-3}$. The $\tilde{t}_{\sigma,ss}$ values reported in Table 2 fall between the heat penetration times from the bottom to the top and from the perimeter to the center. This agreement is reasonable in view of the fact that in the numerical simulation the heat wave has to overcome the flow network as well.

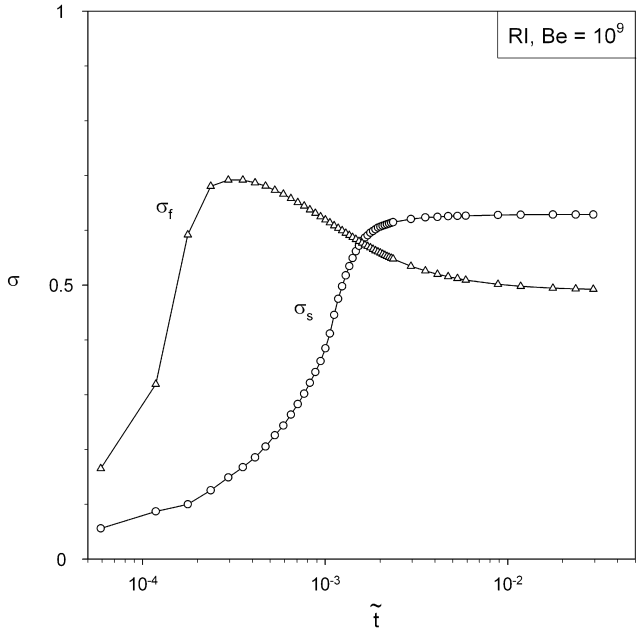


**Fig. 13.** The time evolution of the hot volume fraction of the RI configuration when Be = $10^9$.

**Table 2**
The time required for the hot volume fraction and the peak temperature to reach steady state in the GI and RI configurations when Be = $10^9$.

| | $\tilde{t}_{ss}$ | $\tilde{t}_{\sigma,ss,s}$ | $\tilde{t}_{\sigma,ss,f}$ |
|---|---|---|---|
| GI | $2.67 \times 10^{-2}$ | $1.65 \times 10^{-3}$ | $2 \times 10^{-3}$ |
| RI | $2.27 \times 10^{-2}$ | $1.47 \times 10^{-3}$ | $2.65 \times 10^{-3}$ |

## 6. Conclusions

In this paper we documented the transient heat transfer performance of cooling vasculatures. Four configurations defined by two flow architectures (grids and radial patterns) and two flow directions (from the center to the periphery and from the periphery to the center) compete for short characteristic response time $\tilde{t}_{ss}$, short excess heat removal time $\varepsilon$ and low hot volume fraction $\sigma$.

In Fig. 4 we showed that designs with outlet in the center outperform the designs with inlet in the center because they have noticeable shorter characteristic response times, provided that Be is less than $10^9$. When Be is greater than $10^9$, the main heat transfer mechanism is convection, and this accounts for the minor differences in selecting designs for short characteristic response time. We showed in Fig. 5 that the relationship between the peak temperature and the characteristic response time is $\tilde{T}_{max,ss} \cong 15\tilde{t}_{ss}$.

We also documented the effect of the time delay that separates the cooling process from the start of heating attack. Attractive are the configurations with fast heat removal time: the designs with outlet in the center outperform the designs with inlet in the center. The grids with outlet in the center (GO) have the shortest heat removal time, and the grids with inlet in the center (GI) have the longest heat removal time.

The volume fraction that is at high temperature is an important factor for effective cooling vasculatures. Configurations with low hot volume fractions are sought. When the hot volume fraction of the solid domain $\sigma_s$ is considered, the designs with outlet in the center outperform the designs with inlet in the center patterns. Choosing between grids and radial patterns does not yield significant reductions in the hot volume fraction, Fig. 10. The radial patterns with inlet in the center have the lowest fluid hot volume fraction $\sigma_f$, provided that Be is larger than $10^8$. The time evolution of the hot volume fraction provides an alternative to studying the thermal penetration time of objects with cooling vasculatures.

## Acknowledgements

This work was sponsored by grants from the Air Force Office of Scientific Research and the National Science Foundation.

## References

[1] A. Bejan, S. Lorente, Design with Constructal Theory, Wiley, Hoboken, NJ, 2008.
[2] A. Bejan, Shape and Structure, from Engineering to Nature, Cambridge University Press, Cambridge, UK, 2000.
[3] S.M. Senn, D. Poulikakos, Tree network channels as fluid distributors constructing double-staircase polymer electrolyte fuel cells, J. Appl. Phys. 96 (2004) 842–852.
[4] W. Wechsatol, A. Bejan, S. Lorente, Tree-shaped flow architectures: strategies for increasing optimization speed and accuracy, Numer. Heat Transfer A Appl. 48 (2005) 731–744.
[5] C. Biserni, L.A.O. Rocha, A. Bejan, Inverted fins: geometric optimization of the intrusion into a conducting wall, Int. J. Heat Mass Transfer 47 (2004) 2577–2586.
[6] L.A.O. Rocha, E. Lorenzini, C. Biserni, Geometric optimization of shapes on the basis of Bejan's theory, Int. Commun. Heat Mass Transfer 32 (2005) 1281–1288.

[7] C. Biserni, L.A.O. Rocha, G. Stanescu, E. Lorenzini, Constructal H-shaped cavities according to Bejan's theory, Int. J. Heat Mass Transfer 50 (2007) 2132–2138.
[8] S. Lorente, W. Wechsatol, A. Bejan, Tree-shaped flow structures designed by minimizing path lengths, Int. J. Heat Mass Transfer 45 (2002) 3299–3312.
[9] S. Lorente, A. Bejan, Heterogeneous porous media as multiscale structures for maximum flow access, J. Appl. Phys. 100 (2006) 114909.
[10] A.Y. Alharbi, D.V. Pence, R.N. Cullion, Fluid flow through microscale fractal-like branching channel networks, J. Fluids Eng. 125 (2003) 1051–1057.
[11] X.-Q. Wang, A.S. Mujumdar, C. Yap, Numerical analysis of blockage and optimization of heat transfer performance of fractal-like microchannel nets, J. Electron. Packaging 128 (2006) 38–45.
[12] V.A.P. Raja, T. Basak, S.K. Das, Heat transfer and fluid flow in a constructal heat exchanger, in: Proceedings of the Fifth International Conference on Enhanced, Compact and Ultra-Compact Heat Exchangers: Science, Engineering and Technology, R.K. Shah, M. Ishizuka, T.M. Rudy, V.V. Wadekar (Eds.), Engineering Conferences International, Hoboken, NJ, September 2005.
[13] F. Lundell, B. Thonon, J.A. Gruss, Constructal networks for efficient cooling/heating, in: Second Conference on Microchannels and Minichannels, Rochester, NY, 2004.
[14] Y.S. Muzychka, Constructal design of forced convection cooled microchannel heat sinks and heat exchangers, Int. J. Heat Mass Transfer 48 (2005) 3119–3127.
[15] N. Kockmann, T. Kiefer, M. Engler, P. Woias, Channel networks for optimal heat transfer and high throughput mixers, in: ECI International Conference on Heat Transfer and Fluid Flow in Microscale, Castelvecchio Pascoli, Italy, September 2005.
[16] Y. Chen, P. Cheng, Heat transfer and pressure drop in fractal tree-like microchannel nets, Int. J. Heat Mass Transfer 45 (2002) 2643–2648.
[17] Y. Chen, P. Cheng, An experimental investigation on the thermal efficiency of fractal tree-like microchannel nets, Int. Commun. Heat Mass Transfer 32 (2005) 931–938.
[18] A.K. da Silva, A. Bejan, S. Lorente, Maximal heat transfer density in morphing channels with natural convections, Numer. Heat Transfer A Appl. 45 (2004) 135–152.
[19] M. Lallemand, F. Ayela, M. Favre-Marinet, A. Gruss, D. Maillet, P. Marty, H. Peerhossaini, L. Tadrist, Thermal transfer in micro channels: applications to microexchangers, in: French Congress on Thermics, SFT 2005, Reims, 30 May–2 June, 2005.
[20] Y.S. Muzychka, Constructal multi-scale design of compact micro-tube heat sinks and heat exchangers, Int. J. Therm. Sci. 46 (2007) 245–252.
[21] A.H. Reis, Constructal view of scaling laws of river basins, Geomorphology 78 (2006) 201–206.
[22] A.H. Reis, A.F. Miguel, M. Aydin, Constructal theory of flow architecture of the lungs, J. Med. Phys. 31 (2004) 1135–1140.
[23] A. Bejan, J.H. Marden, Constructing animal locomotion from new thermodynamics theory, Am. Sci. 94 (2006) 342–349.
[24] A.H. Reis, Constructal theory from engineering to physics and how flow systems develop shape and structure, Appl. Mech. Rev. 59 (2006) 269–282.
[25] A. Bejan, S. Lorente, Constructal theory of generation of configuration in nature and engineering, J. Appl. Phys. 100 (2006) 041301.
[26] A. Bejan, S. Lorente, K.-M. Wang, Networks of channels for self-healing composite materials, J. Appl. Phys. 100 (2006) 033528.
[27] S. Kim, S. Lorente, A. Bejan, Vascularized materials: tree-shaped flow architectures matched canopy to canopy, J. Appl. Phys. 100 (2006) 063525.
[28] S.R. White, N.R. Sottos, J. Moore, P. Geubelle, M. Kesseler, E. Brown, S. Suresh, S. Viswanathan, Autonomic healing of polymer composites, Nature 409 (2001) 794–797.
[29] K.-M. Wang, S. Lorente, A. Bejan, Vascularized networks with two optimized channel sizes, J. Phys. D Appl. Phys. 39 (2006) 3086–3096.
[30] K.-M. Wang, S. Lorente, A. Bejan, Vascularization with grids of channels: multiple scales, loops and body shapes, J. Phys. D Appl. Phys. 40 (2007) 4740–4749.
[31] S. Kim, S. Lorente, A. Bejan, W. Miller, J. Morse, The emergence of vascular design in three dimensions, J. Appl. Phys. 103 (2008) 123511.
[32] J. Lee, S. Kim, S. Lorente, A. Bejan, Vascularization with trees matched canopy to canopy: diagonal channels with multiple sizes, Int. J. Heat Mass Transfer 51 (2008) 2029–2040.
[33] S. Kim, S. Lorente, A. Bejan, Vascularized materials with heating from one side and coolant forced from the other side, Int. J. Heat Mass Transfer 50 (2007) 3498–3506.
[34] S. Kim, S. Lorente, A. Bejan, Dendritic vascularization for countering intense heating from the side, Int. J. Heat Mass Transfer 51 (2008) 5877–5886.
[35] K.-M. Wang, S. Lorente, A. Bejan, Vascular material cooled with grids and radial channels, Int. J. Heat Mass Transfer 52 (2009) 1230–1239.
[36] S. Bhattacharjee, W.L. Grosshandler, The formation of a wall jet near a high temperature wall under microgravity environment, ASME HTD 96 (1988) 711–716.
[37] S. Petrescu, Comments on the optimal spacing of parallel plates cooled by forced convection, Int. J. Heat Mass Transfer 37 (1994) 1283.
[38] Available from: <http://www.fluent.com>.
[39] S. Lorente, A. Bejan, Svelteness freedom to morph and constructal multi-scale flow structures, Int. J. Therm Sci. 44 (2005) 1123–1130.